Decimetre-scaled spectrophotometric properties of the nucleus of comet 67P/Churyumov–Gerasimenko from OSIRIS observations

Clément Feller, Sonia Fornasier, Pedro Henrique Hasselmann, Antonella Barucci, Frank Preusker, Frank Scholten, Laurent Jorda, Antoine Pommerol, Bernhard Jost, Olivier Poch, et al.

Monthly Notices
of the
ROYAL ASTRONOMICAL SOCIETY

MNRAS **462,** S287–S303 (2016)
Advance Access publication 2016 October 21

doi:10.1093/mnras/stw2511

Decimetre-scaled spectrophotometric properties of the nucleus of comet 67P/Churyumov–Gerasimenko from OSIRIS observations

C. Feller,[1⋆] S. Fornasier,[1⋆] P. H. Hasselmann,[1⋆] A. Barucci,[1] F. Preusker,[2] F. Scholten,[2] L. Jorda,[3] A. Pommerol,[4] B. Jost,[4] O. Poch,[4] M. R. ElMaary,[4] N. Thomas,[4] I. Belskaya,[5] M. Pajola,[6,7] H. Sierks,[8] C. Barbieri,[9] P. L. Lamy,[10] D. Koschny,[11] H. Rickman,[12,13] R. Rodrigo,[14,15] J. Agarwal,[8] M. A'Hearn,[16] J.-L. Bertaux,[17] I. Bertini,[7] S. Boudreault,[8] G. Cremonese,[18] V. Da Deppo,[19] B. J. R. Davidsson,[20] S. Debei,[21] M. De Cecco,[22] J. Deller,[8] M. Fulle,[23] A. Giquel,[8] O. Groussin,[3] P. J. Gutierrez,[24] C. Güttler,[8] M. Hofmann,[8] S. F. Hviid,[2] H. Keller,[25] W.-H. Ip,[26] J. Knollenberg,[2] G. Kovacs,[8] J.-R. Kramm,[8] E. Kührt,[2] M. Küppers,[27] M. L. Lara,[25] M. Lazzarin,[9] C. Leyrat,[1] J. J. Lopez Moreno,[25] F. Marzari,[9] N. Masoumzadeh,[8] S. Mottola,[2] G. Naletto,[28,7,19] D. Perna,[1] N. Oklay,[8] X. Shi,[8] C. Tubiana[8] and J.-B. Vincent[8]

Affiliations are listed at the end of the paper

Accepted 2016 September 29. Received 2016 September 27; in original form 2016 July 5

ABSTRACT

We present the results of the photometric and spectrophotometric properties of the 67P/Churyumov–Gerasimenko nucleus derived with the Optical, Spectroscopic and Infrared Remote Imaging System instrument during the closest fly-by over the comet, which took place on 2015 February 14 at a distance of ∼6 km from the surface. Several images covering the 0°–33° phase angle range were acquired, and the spatial resolution achieved was 11 cm pixel^{-1}. The flown-by region is located on the big lobe of the comet, near the borders of the Ash, Apis and Imhotep regions. Our analysis shows that this region features local heterogeneities at the decimetre scale. We observed difference of reflectance up to 40 per cent between bright spots and sombre regions, and spectral slope variations up to 50 per cent. The spectral reddening effect observed globally on the comet surface by Fornasier et al. (2015) is also observed locally on this region, but with a less steep behaviour. We note that numerous metre-sized boulders, which exhibit a smaller opposition effect, also appear spectrally redder than their surroundings. In this region, we found no evidence linking observed bright spots to exposed water-ice-rich material. We fitted our data set using the Hapke 2008 photometric model. The region overflown is globally as dark as the whole nucleus (geometric albedo of 6.8 per cent) and it has a high porosity value in the uppermost layers (86 per cent). These results of the photometric analysis at a decimetre scale indicate that the photometric properties of the flown-by region are similar to those previously found for the whole nucleus.

Key words: methods: data analysis – space vehicles – space vehicles: instruments – techniques: image processing – techniques: photometric – comets: individual: 67P/Churyumov–Gerasimenko.

1 INTRODUCTION

The *Rosetta* mission is the cornerstone mission of the European Space Agency devoted to the study of the minor bodies of the Solar system. Its primary objective is to perform an extensive study of the comet 67P/Churyumov–Gerasimenko (hereafter 67P/CG), of

⋆ E-mail: clement.feller@obspm.fr (CF); sonia.fornasier@obspm.fr (SF); pedro.hasselmann@obspm.fr (PHH)

its nucleus as well as the contiguous cometary environment with the help of several instruments, including cameras, spectrometers, dust analysers and radio science experiments.

Previous space missions designed for comets exploration have helped building up an awesome trove of knowledge of those objects, yet the spacecrafts only performed fly-by manoeuvres (we refer the reader to A'Hearn et al. (2005), A'Hearn et al. (2011), Barucci, Dotto & Levasseur-Regourd (2011) and references therein). The *Rosetta* mission is the first one to escort a comet from 4 au inbound, through its perihelion (1.24 au in the case of 67P/CG) and back to 3 au outbound, as well as the first one to have executed a fly-by manoeuvre about 6 km above a cometary nucleus.

The Optical, Spectroscopic and Infrared Remote Imaging System (OSIRIS) instrument is the scientific camera system on-board the *Rosetta* orbiter.

This imaging system has allowed us to perform extensive studies of the 67P/CG nucleus. Beyond depicting a peculiar bilobate shape, OSIRIS has characterized a surface exhibiting a complex morphology, including both fragile and consolidated rocky terrains, dusty regions, depressions and pits, sometime active, and extensive layering (Massironi et al. 2015; Sierks et al. 2015; Thomas et al. 2015b; Vincent et al. 2015). Photometric and spectrophotometric properties of the 67P/CG comet were studied by Fornasier et al. (2015), La Forgia et al. (2015), Oklay et al. (2016), Lucchetti et al. (2016) and Pajola et al. (2016). In Fornasier et al. (2015), the authors reported a globally red spectral behaviour for the nucleus, consistent with that of primitive Solar system bodies like Jupiter Trojans (Fornasier et al. 2004, 2007) and part of the trans-neptunian population (Fornasier et al. 2009). They found colour and albedo heterogeneities over the nucleus. Three kind of terrains were identified on the basis of the spectral slope, those having a bluer (i.e. a less steep spectral slope value) being associated with areas enriched in water-ice content, and those having a higher spectral slope value were found predominantly to correspond to dust-rich regions.

The comet is dark: its geometric albedo reaches 6.5 per cent at 649 nm, and at a decametre scale, we observed local reflectance variations up to 25 per cent (Fornasier et al. 2015). The VIRTIS spectrometer results indicate a global surface composition dominated by dehydrated and organic-rich refractory materials (Capaccioni et al. 2015). However, several local bright spots were identified in the OSIRIS images (Pommerol et al. 2015b; Fornasier et al. 2016; Barucci et al. 2016; Oklay et al. 2016) and interpreted as exposures of water-ice. The presence of water-ice has been confirmed by the VIRTIS observations in the Hapi and Imhothep regions, and in some of the bright spots (De Sanctis et al. 2015; Filacchione et al. 2016; Barucci et al. 2016).

In this work, we investigate the photometric and spectrophotometric properties of the comet 67P/CG's nucleus based on a data set of images, taken by the OSIRIS imaging system, with the best spatial resolution (11 cm pixel^{-1}) since the S/C had started to escort the comet, and in which the phase angle ranges from 0° up to 33°. We sought thus to study the heterogeneity of the nucleus at the decimetre scale and to constraint parameters modelling the surge of intensity of the reflected light at low phase angles.

The following section presents the instrument and the observations in question, and the third one summarizes the steps of data reduction and preparation. In the fourth and fifth sections, we shall present the results of our spectrophotometric analyses examining, first, the flown-by region as a whole, and then considering parts of this region. After which we shall present the results of our photometric analysis in the sixth section. We discuss the results of our analyses in the seventh section.

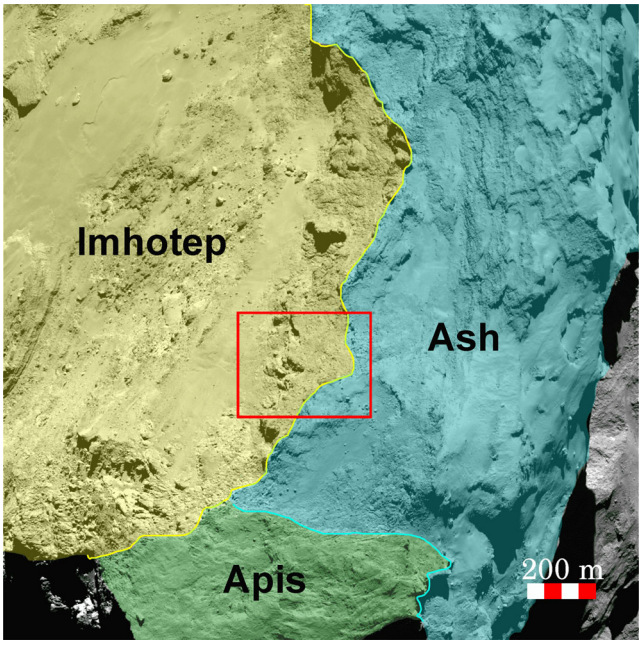

Figure 1. WAC image taken on 2015 February 14 at UTC – 14:36:55 depicting the fly-by area (red square) and the surroundings morphological regions. The scale in the middle of the image is of 0.92 m pixel^{-1}. The dimensions of the red square are about 350 m per 225 m.

2 OBSERVATIONS

The OSIRIS imaging system comprises two cameras: the Narrow-Angle Camera (hereafter NAC) and the Wide-Angle Camera (hereafter WAC). The NAC has a field of view of 2.°35 × 2.°35, it was designed to perform observations of the nucleus with broad-band filters ranging from the near UV to the near-IR domains (240–1000 nm) at an angular resolution of 18.6 μrad pixel^{-1}. Those filters are optimized for the study of the nucleus' mineralogy. The WAC has a field of view of 11.°6 × 12.°1, and was designed to perform observations of the dust and gaseous species in the coma in the same wavelength domain (250–1000 nm) though with narrow-band filters at an angular resolution of 101 μrad pixel^{-1}.

Both cameras are equipped with the same detector system: a 2048 × 2048 pixels array CCD with a pixel size of 13.5 μm. For more detailed description of the instrument, we refer the reader to Keller et al. (2007).

On 2015 February 14, the *Rosetta* spacecraft flew over the Imhotep region, and the closest approach took place close to the boundary between Ash, Apis and Imhotep, as depicted in Fig. 1. For detailed descriptions of the definition of the comet's morphological and structural regions, we refer the reader to Thomas et al. (2015a) and El-Maarry et al. (2015).

Around the time of closest approach, the OSIRIS instrument took series of observations using several filters with both NAC and WAC cameras. For the NAC, those observations were performed using two sets of filters: 23 series of observations with 3 filters (namely *F*82, *F*84 and *F*88), and 2 series of observations with all the 11 NAC filters (see Tables 1 and 2).

The WAC took series of observations using only two filters (one centred at 375.6 nm, another at 631.6 nm). However, as multiple shutter errors plagued the WAC during the fly-by, we did not include those images in our analysis.

At that epoch, the comet was 2.31 au away from the Sun and according to the trajectory and attitude reconstruction in the frame

Table 1. Table listing the OSIRIS filters' name, with the associated central wavelength and bandwidth, present in this data set.

NAC filter	Wavelength (nm)	Bandwidth (nm)
*F*15	269.3	53.6
*F*16	360.0	51.1
*F*84	480.7	74.9
*F*83	535.7	62.4
*F*82	649.2	84.5
*F*27	701.2	22.1
*F*88	743.7	64.1
*F*51	805.3	40.5
*F*41	882.1	65.9
*F*61	931.9	34.9
*F*71	989.3	38.2

of the Cheops boulder (Preusker et al. 2015b), the median distance between the spacecraft and the part of the nucleus surface apparent in the NAC field of view varies between $5.711^{+0.265}_{-0.090}$ and $6.737^{+0.310}_{-0.015}$ km. The minimum distance was attained at 12:39:54 (Fig. 2). The variations of the uncertainties displayed in this figure are due to the dispersion of the values as the camera's field of view pans different parts of the flown-by region. The median phase angle in the frame

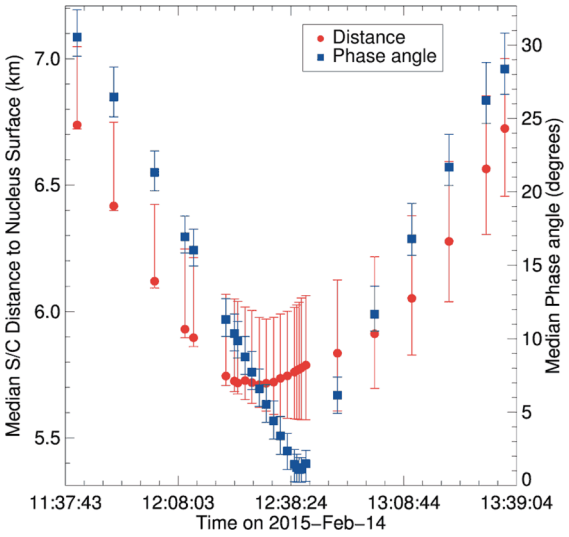

Figure 2. Variations of the median phase angle and distance of the spacecraft to the surface variations during the fly-by. The bars around the median values correspond to the computed extrema according to the 3D model.

Table 2. List of the NAC observations analysed. The time column corresponds to the epoch at which the first observation of the sequence was taken. The values indicated in the last three columns correspond to the median values and their dispersion over the NAC field of view computed while producing simulations of the NAC observations with a specific 3D shape model of the region flown-by produced by the DLR.

Time (UTC)	NAC filters	Median phase angle (°)	Spacecraft median distance to nucleus surface (km)	Median resolution (m pixel^{-1})
2015-02-14T11:40:54	*F*82, *F*84, *F*88	30.5 ± 1.4	6.73 ± 0.05	0.126 ± 0.001
2015-02-14T11:50:45	*F*82, *F*84, *F*88	26.4 ± 1.4	6.41 ± 0.07	0.120 ± 0.001
2015-02-14T12:01:44	*F*82, *F*84, *F*88	21.3 ± 1.2	6.12 ± 0.08	0.115 ± 0.001
2015-02-14T12:09:54	*F*15, *F*16, *F*82, *F*83,	16.9 ± 1.1	5.93 ± 0.08	0.111 ± 0.001
–	*F*84, *F*27, *F*88, *F*41,	–	–	–
–	*F*61, *F*71, *F*51	–	–	–
2015-02-14T12:12:12	*F*82, *F*84, *F*88	16.0 ± 1.1	5.89 ± 0.08	0.111 ± 0.001
2015-02-14T12:20:54	*F*15, *F*16, *F*82, *F*83,	11.3 ± 1.1	5.74 ± 0.08	0.108 ± 0.001
–	*F*84, *F*27, *F*88, *F*41,	–	–	–
–	*F*61, *F*71, *F*51	–	–	–
2015-02-14T12:23:12	*F*82, *F*84, *F*88	10.3 ± 1.0	5.72 ± 0.08	0.107 ± 0.001
2015-02-14T12:24:05	*F*82, *F*84, *F*88	9.8 ± 1.0	5.71 ± 0.08	0.107 ± 0.001
2015-02-14T12:26:05	*F*82, *F*84, *F*88	8.7 ± 1.0	5.72 ± 0.08	0.107 ± 0.001
2015-02-14T12:27:54	*F*82, *F*84, *F*88	7.7 ± 1.0	5.71 ± 0.09	0.107 ± 0.001
2015-02-14T12:29:54	*F*82, *F*84, *F*88	6.6 ± 0.9	5.71 ± 0.09	0.107 ± 0.001
2015-02-14T12:31:45	*F*82, *F*84, *F*88	5.5 ± 0.9	5.71 ± 0.10	0.107 ± 0.002
2015-02-14T12:33:45	*F*82, *F*84, *F*88	4.4 ± 0.8	5.72 ± 0.11	0.107 ± 0.002
2015-02-14T12:35:34	*F*82, *F*84, *F*88	3.3 ± 0.8	5.73 ± 0.11	0.107 ± 0.002
2015-02-14T12:37:25	*F*82, *F*84, *F*88	2.3 ± 0.7	5.74 ± 0.12	0.108 ± 0.002
2015-02-14T12:39:19	*F*82, *F*84, *F*88	1.4 ± 0.6	5.76 ± 0.12	0.108 ± 0.002
2015-02-14T12:39:58	*F*82, *F*84, *F*88	1.2 ± 0.5	5.76 ± 0.12	0.108 ± 0.002
2015-02-14T12:40:34	*F*82, *F*84, *F*88	1.0 ± 0.5	5.77 ± 0.12	0.108 ± 0.002
2015-02-14T12:41:11	*F*82, *F*84	1.1 ± 0.5	5.77 ± 0.12	0.108 ± 0.002
2015-02-14T12:42:25	*F*82	1.4 ± 0.6	5.78 ± 0.12	0.108 ± 0.002
2015-02-14T12:50:54	*F*82, *F*84, *F*88	6.1 ± 0.8	5.83 ± 0.12	0.109 ± 0.002
2015-02-14T13:00:54	*F*82, *F*84, *F*88	11.6 ± 1.3	5.91 ± 0.11	0.111 ± 0.002
2015-02-14T13:10:54	*F*82, *F*84, *F*88	16.7 ± 1.6	6.05 ± 0.12	0.113 ± 0.002
2015-02-14T13:20:54	*F*82, *F*84, *F*88	21.6 ± 1.6	6.27 ± 0.13	0.118 ± 0.002
2015-02-14T13:30:54	*F*82, *F*84, *F*88	26.2 ± 1.8	6.56 ± 0.13	0.123 ± 0.002
2015-02-14T13:35:54	*F*82, *F*84, *F*88	28.3 ± 1.9	6.72 ± 0.12	0.126 ± 0.002

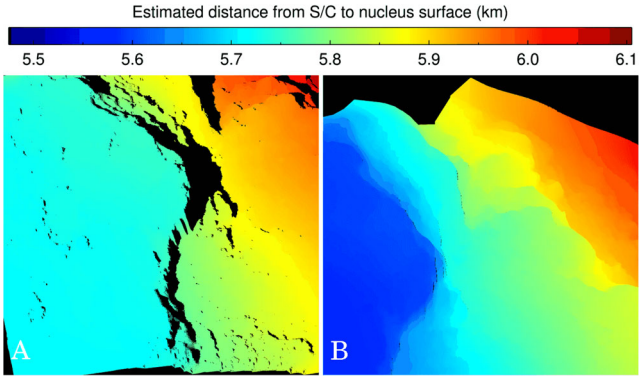

Figure 3. Computed depth maps with the 3D model at UTC – 12:20:54 (left) and at UTC – 12:39:25 (right) as perceived from the *Rosetta* spacecraft. The black areas correspond either to shadows or to regions not defined in the 3D model of the region.

of the CCD varies between $1\overset{\circ}{.}09\ ^{+0\overset{\circ}{.}82}_{-1\overset{\circ}{.}09}$ and $30\overset{\circ}{.}5\ ^{+1\overset{\circ}{.}9}_{-1\overset{\circ}{.}3}$. The NAC field of view being $2\overset{\circ}{.}35 \times 2\overset{\circ}{.}35$ wide, the comet surface was observed with a decimetre resolution and at a phase angle of zero between 12:39:58 (UTC) and 12:42:25 (UTC), as confirmed by the presence of the penumbra of *Rosetta* in the corresponding images (see Fig. 4e).

The region flown-by has been identified as a part of the boundary between the morphological regions Ash and Imhotep. A dedicated 3D model of the region has been generated from this data set (Preusker et al. 2015a). In the Cheops frame, this region extends from $-170\overset{\circ}{.}12$ to $178\overset{\circ}{.}99$ in longitude, from $5\overset{\circ}{.}41$ to $14\overset{\circ}{.}31$ in latitude, and from 1.954 to 2.445 km in distance from the nucleus centre of mass.

This analysed area is a transition region located between the fine deposits on the layered terrain unit (distance $\leq$5.75 km, in Fig. 3A) and the outcropping layered terrain unit (distance $\geq$ 5.7 km, in Fig. 3B) presented in Giacomini et al. (2016). The clear and unambiguous morphological limit which is here present, is the main reason for the distinction between the two separate geographical regions, i.e. the Ash region and the Imhotep depression (El-Maarry et al. 2015). As from Massironi et al. (2015, see the extended data in Fig. 2e), the studied area clearly shows the presence of metre to centimetre scale strata heads pointing towards Imhotep. Such strata are almost continuously present in the 500 m steep cliff, demonstrating that the proposed layered structure of 67P/CG is not only detectable on a global scale, but also on the highest resolution images.

3 DATA REDUCTION

The images used for this study were reduced using the OSIRIS standard pipeline (OSICALLIOPE v.1.0.0.21) up to level 3B, following the data reduction steps described in Küppers et al. (2007) and Tubiana et al. (2015).

Those steps include correction for bias, flat-field and geometric distortion and absolute flux calibration (in W m^{-2} nm^{-1} sr^{-1}).

The last step of the calibration transforms the images in radiance factor (hereafter noted RADF). The radiance factor was notably defined in Hapke (1993), we computed it here according to the following formula:

$$\mathrm{RADF}(\lambda) = \frac{\pi \cdot I(\lambda)}{\mathrm{F}_{\odot}(\lambda, r)} \quad (1)$$

where I is the observed scattered radiance and $\mathrm{F}_{\odot}$ the incoming solar irradiance at the heliocentric distance r of the comet. The solar irradiance $\mathrm{F}_{\odot}(\lambda, r)$ is wavelength dependent and it was calculated at the central wavelength of each filter to be consistent with the methodology applied to derive the absolute calibration factors.

For the spectrophotometric analysis, we first coregistered the images of a given observing sequence using the images acquired with the *F*82 NAC filter (centred at 649.2 nm) as reference. A PYTHON script was developed to perform the coregistration based on an adaptation of the PYTHON code described in Van Der Walt et al. (2014).

We then generated simulated images of the solar incidence, emission and phase angles used for the photometric correction of the data. A 3D shape model of the region flown-by was created following the same procedure described in Preusker et al. (2015b). This model was used alongside SPICE kernels (Acton 1996) of the reconstructed trajectory of the spacecraft produced by the *Rosetta* flight dynamics team of ESA and the Optimised Astrophysical Simulator for Imaging Systems (Jorda et al. 2010; Hasselmann et al. 2016) to retrieve the illumination conditions of each facet of the shape model.

Those informations were employed to produce a photometric correction of the data. For the spectrophotometric analysis, we correct the images for the illuminations conditions by applying the Lommel–Seeliger disc law:

$$D(i, e, a) = \frac{2\mu_{\mathrm{i}}}{\mu_{\mathrm{e}} + \mu_{\mathrm{i}}}, \quad (2)$$

where μ_{i} and μ_{e} are, respectively, the cosine of the solar incidence (i) and emission (e) angles.

Three-colours images (or hereafter RGB) were generated from the observations with the NAC filters centred at 743.7 nm (R), 649.2 nm (G) and 480.7 nm (B). These images were simply coregistered, no photometric corrections were applied to them. The RGBs were produced with the so-called STIFF program (Bertin 2011). Figs 4(a) and (d) present two of the generated colour-stretched RGB from the presented data set, in order to investigate colour heterogeneities over the surface.

The spectral slope was computed using the following formula:

$$S[\text{per cent}/100\,\text{nm}] = \frac{R_{743\,\mathrm{nm}} - R_{535\,\mathrm{nm}}}{R_{535\,\mathrm{nm}}} \times \frac{10^4}{(743.7\,[\mathrm{nm}] - 535.7\,[\mathrm{nm}])}, \quad (3)$$

where R_{i} is the radiance factor at a given wavelength. We choose to maintain the normalization at 535.7 nm (*F*83 filter), even for sequences where we do not have direct measurements with the *F*83 filter, to be coherent with previous studies on the comet and literature data. Thus, for the three filters sequences, we estimated the 535.7 nm flux for each pixel through a linear regression of the data acquired between 480.7 and 649.2 nm.

4 GLOBAL ANALYSIS OF THE FLOWN-BY REGION

The global spectrophotometric and photometric properties of the nucleus but also the surroundings of the flown-by region have been previously investigated by Fornasier et al. (2015, see figs. 9, 13, and 14) on the first resolved images of the comet acquired on 2014 July–August, at 3.6 au of heliocentric distance. The surroundings of the flown-by region were classed as belonging to the group of terrains with the highest spectral slope (i.e. the reddest) and, in the

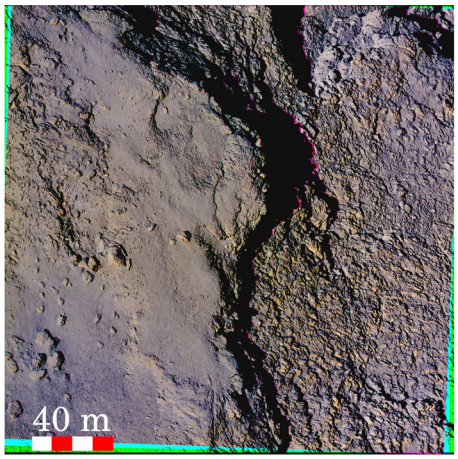

(a) RGB map generated from the 12:20:54's sequence of observations

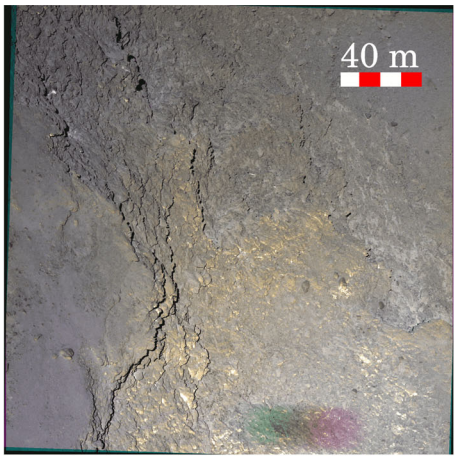

(d) RGB map generated from the 12:39:58's sequence of observations

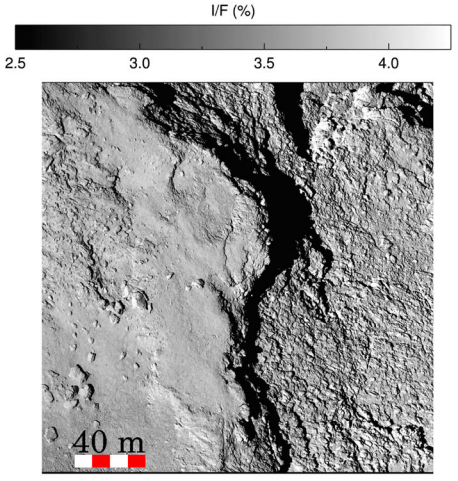

(b) NAC Orange filter image taken at 12:20:54

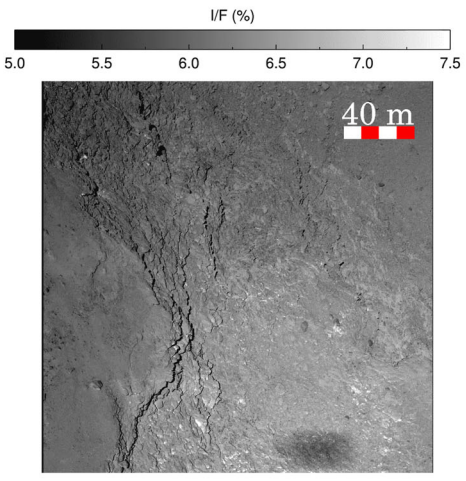

(e) NAC Orange filter image taken at 12:39:58

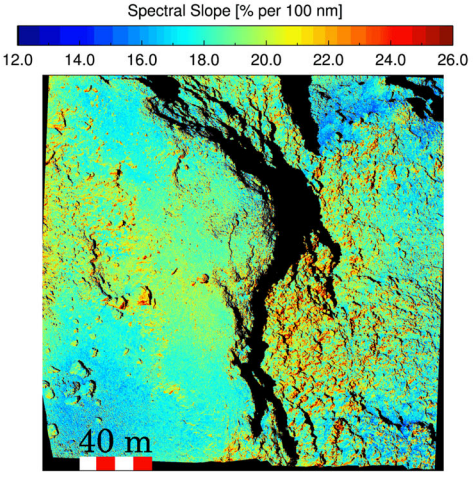

(c) Spectral slope mapping computed from the 12:20:54's observations

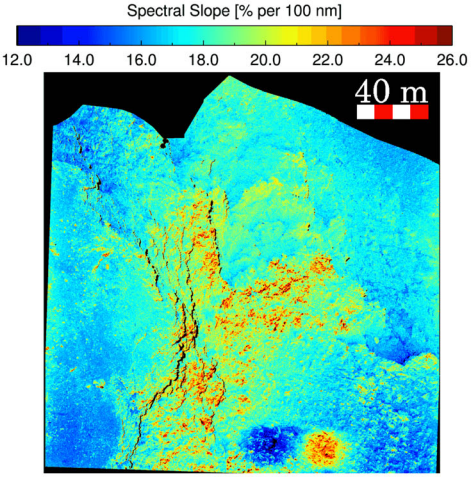

(f) Spectral slope mapping computed from the 12:39:25's observations

Figure 4. RGB, I/F images, and spectral slope mappings from the 12:20:54 and 12:39:25 sequences of observations. In panel e, as explained previously in the article, the dark area at the bottom of the image corresponds to the penumbra due to the *Rosetta* spacecraft. The artefact at the bottom of panels d and f is due to the motion of the penumbra as the observations are taken.

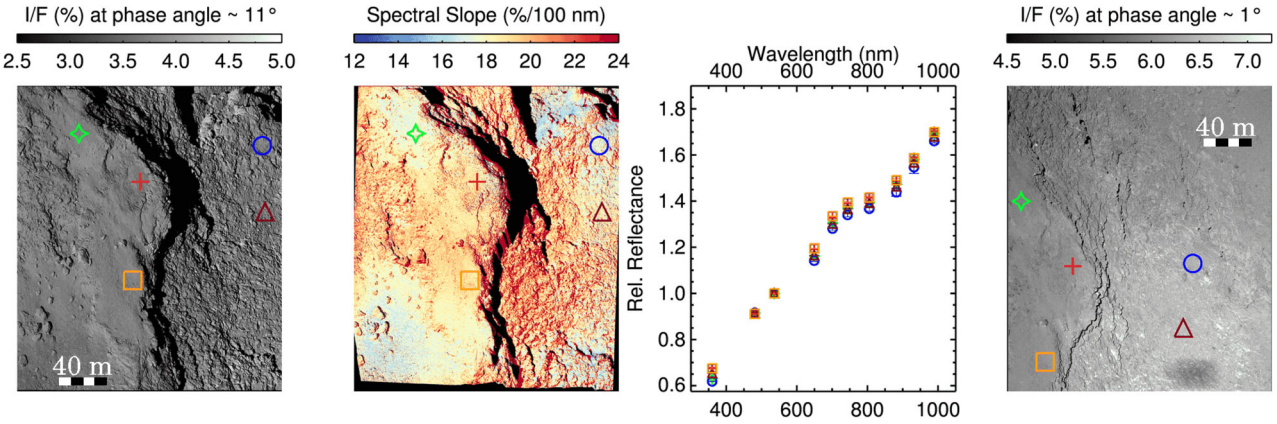

Figure 5. From left to right: radiance factor of the flown-by region, associated spectral slope map (evaluated in the 743–535 nm range) and spectrophotometry for six selected features at phase angle 11° (NAC *F*22 image UTC – 12:20:54). The last figure on the right presents the radiance factor at phase ∼1° (NAC *F*22 image UTC – 12:39:54) is also represented. The phase curves of the violet triangle and orange square measurements are presented in Fig. 13.

882.1–535.7 nm range, they were observed to have a spectral slope value >14 per cent/(100 nm) at phase angle 1°.3, and >18 per cent/(100 nm) at phase angle 50°. The reader is referred to figs 14 and 9 in the aforementioned article for more details.

Fig. 4 depicts the RGB colours, reflectance and spectral slope maps of areas observed at 12:20:54 and 12:39:58. The surface clearly shows local reflectance and colour/spectral slope values variations, with the presence of several bright spots, sombre boulders and some striae, confirming that the surface is heterogeneous at several scales. Brightness variations in the comet's surface at centimetre and millimetre scale were reported by the CIVA instrument[1] on-board the Philae lander (Bibring et al. 2015), which observed a surface globally dominated by dark conglomerate, likely made of organics, with the presence of brighter spots that may be linked to mineral grains or pointing to ice-rich material. Heterogeneities, reported by Fornasier et al. (2015), were observed at a larger scale (>2 m pixel^{-1}).

From the February 14 images, we find a median reflectance of 6.15 ± 0.07 per cent (cf. Fig. 4e) in the *F*82 filter image taken at 12:39:58. The sombre boulders show a reflectance ∼10 per cent lower than the average value while the brightest regions show a reflectance about 20 per cent higher. However, in this flown-by region, we do not see strong variations (i.e. a factor 2 or higher) in reflectance as observed for bright spots and ice-rich regions on different areas of the nucleus (Pommerol et al. 2015b; Barucci et al. 2016; Fornasier et al. 2016; Oklay et al. 2016).

The most remarkable changes are observed in the images taken when the phase angle is minimal, such as in Fig. 4(e). In particular, we notice several boulders, metre-sized and sub-metre-sized, located on both sides of the region, whose reflectance is lower than that of their surroundings at small phase angle observations. We determined that the phase functions of those boulders are different from that of observed bright spots, or even the immediate surroundings of such features. This particular result is discussed in the next section alongside the photometric analysis of the entire region (cf. Fig. 13 and Table 5).

The RGB images (see Figs 4a and d) indicate redder colours along the cliff in Fig. 4(a), and along the cliff, terraces and outcrops in Fig. 4(d). In this image, the green to red artefact in the bottom is simply the shadow projected by the *Rosetta* spacecraft. Similarly, the receding of the projected shadows and the motion of the S/C also left artefacts in the RGB. Such elements on surface of the nucleus were not further considered.

In those colour-stretched RGBs, we note that most of the previously spotted bright patches and striae of surface appear to be located where the nucleus surface looks redder. This is confirmed by the spectral slope mappings (in the 743–535 nm range, Figs 4c and f), where the aforementioned red features display indeed a strong spectral slope (above 21 per cent/100 nm). Spectral slopes values are found to vary between 15 and 23 per cent/(100 nm) at phase angle ∼1° (UTC: 12:39:58, cf. Fig. 10), confirming that the flown-by region is one of the redder of the comet's surface.

The spectral slope mappings evolution computed at different epochs of the fly-by is represented in Fig. 10 and the corresponding phase-reddening effect is discussed in Section 5.1 and summarized by Fig. 11.

We investigated the spectrophotometric properties of the surface on several relatively smooth areas visible on multiple sequences and on both morphological regions, and where no boulders are discernible at the decimetre scale. We considered the observations related to the 12:20:54 and 12:39:58 sequences. The integrated radiance factor inside boxes of 15 × 15 pixels (i.e. about 1.5 × 1.5 m^2 on the nucleus) is presented in Fig. 5. We note that, at every wavelength, the variations of the measured relative reflectances are, in average, of 3.5 ± 2.1 per cent. Furthermore, in the 743–535.5 nm range, the median spectral slope of those measurements is found to be equal to (17.7 ± 1.0) per cent/100 nm. Hence, the smooth terrains investigated over the two different morphological regions were not found to be distinctly different.

We also note an increase of the flux in the 700–750 nm region, as already seen in Fornasier et al. (2015) analysis. This feature is not related to the nucleus surface properties but it has been linked to cometary activity and attributed to H_2O^+ and/or NH_2 emission in the very inner coma (Fornasier et al. 2015). As our observations are mostly carried out in three filters, including the one centred to 743 nm, we need to estimate the cometary emission effects in the spectral slope value evaluated in the 743–535 nm range compared to the one evaluated in the 882–535 nm wavelength range, and used in the literature for the 67P/CG comet (Fornasier et al. 2015; La Forgia et al. 2015; Oklay et al. 2016; Pajola et al. 2016). We thus

[1] CIVA stands for Comet Infrared and Visible Analyser.

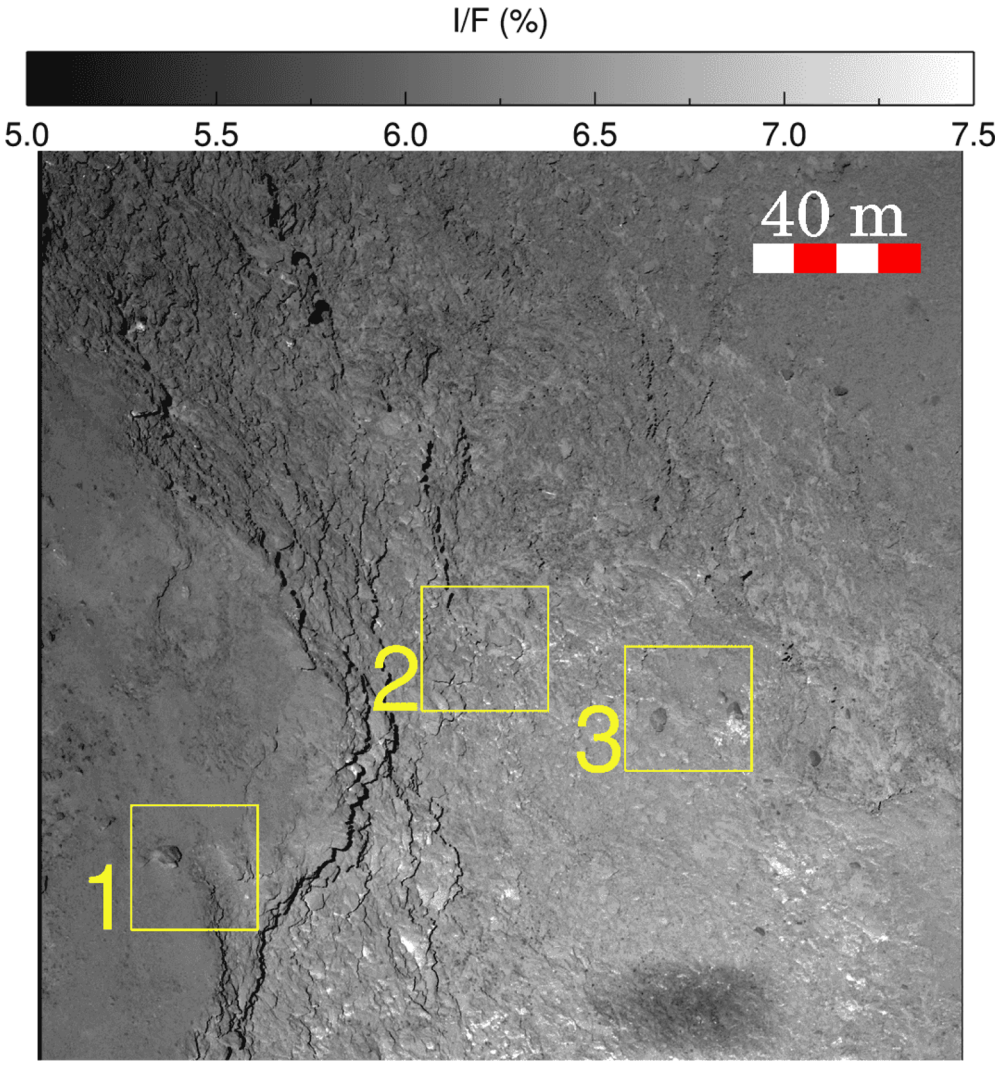

Figure 6. NAC orange filter image taken at UTC – 12:39:58 with the relative locations of ROI.

computed the spectral slopes for those investigated terrains, in both those wavelength ranges, for the observations acquired at 12:09:54 and 12:20:54, where the full set of NAC filters is available. We found that the spectral slopes computed in the 743–535 nm range are about 24 per cent higher than those computed in the 882–535 nm range, thus indicating an important contribution of the cometary emission. The different spectral wavelength range used and the cometary emission contribution in the 743–535 nm spectral slope must be taken into account when comparing spectral slopes values reported in the literature.

When considering the reflectance maps of Figs 4(b) and (e) more closely, we observe numerous local heterogeneities in terms of absolute reflectance and of spectral slope value, that we discuss in the following section.

5 REFLECTANCE AND SPECTRAL BEHAVIOUR OF LOCAL FEATURES

For this analysis, we sought surface elements, which were visible in almost every single sequence of observations, and which also exhibited heterogeneities in terms of absolute reflectance and of spectral slopes. We investigate here three such regions of interests (ROI), which are indicated in Fig. 6. The first ROI is over the Ash region and includes two metre-scale boulders as well as a spot(the violet triangle in Fig. 7) which appears bright on every filter image of the data set. The second ROI delimits a part of the Imhotep region including a strata head which appears dark and presents a red spectral behaviour (site B in Fig. 8) as well as an outcrop exhibiting a bluer spectral behaviour (site C in the same figure). Finally, in the third ROI, we investigated a couple of boulders which clearly appear darker than the surroundings at small phase angle (sites D and F in Fig. 9).

More in detail, ROI no. 1 of Fig. 6 is the clear example of the fine deposits on the layered terrain, this being demonstrated by the eroded niche margin on the right-hand side, unveiling a set of centimetre-scale layers. ROI no. 2 focuses on the decimetre-scale layers with the possible presence of detaching blocks, as observed in Hathor region, but on different scales (Pajola et al. 2015). Finally, ROI no. 3 corresponds to a specific area with a cluster of boulders. The origin of this kind of boulders has not been here investigated, and it is not the purpose of this work, none the less, since there is a cliff in close proximity it is not unreasonable to think that they may have detached from it, as observed and confirmed on many other locations on 67P/CG (Pajola et al. 2016).

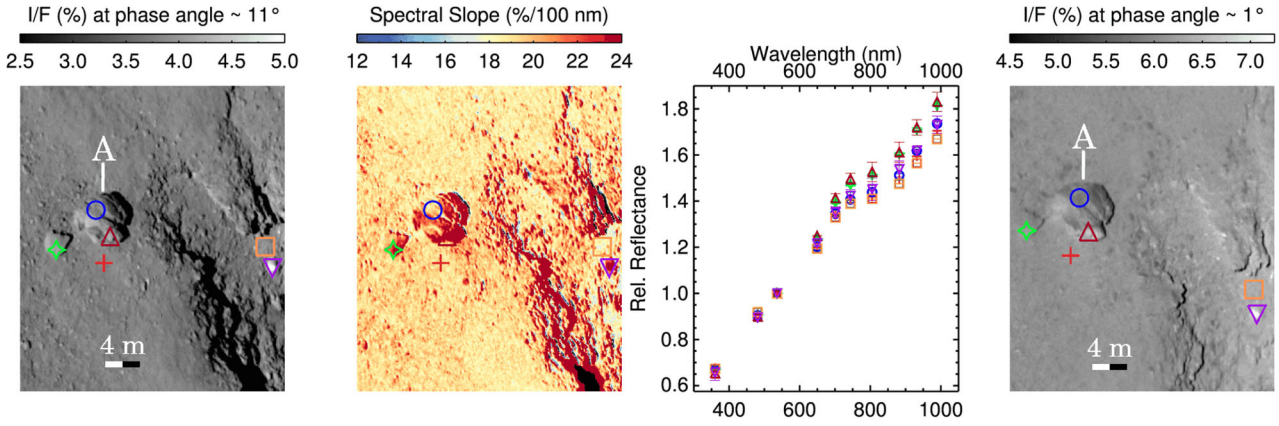

Figure 7. From left to right: radiance factor of ROI 1, associated spectral slope map (evaluated in the 743–535 nm range) and spectrophotometry for six selected features at phase angle 11° (NAC orange filter UTC – 12:20:54). Radiance factor at phase ∼1° (NAC orange filter UTC – 12:39:54).

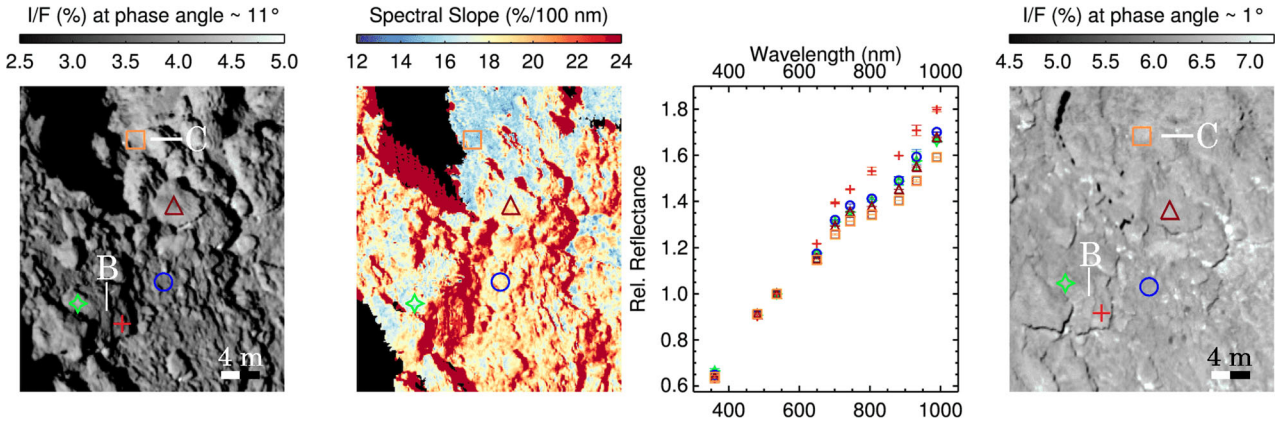

Figure 8. From left to right: radiance factor of ROI 2, associated spectral slope map (evaluated in the 743–535 nm range) and spectrophotometry for five selected features at phase angle 11° (NAC orange filter UTC – 12:20:54). Radiance factor at phase ∼1° (NAC orange filter UTC – 12:39:54).

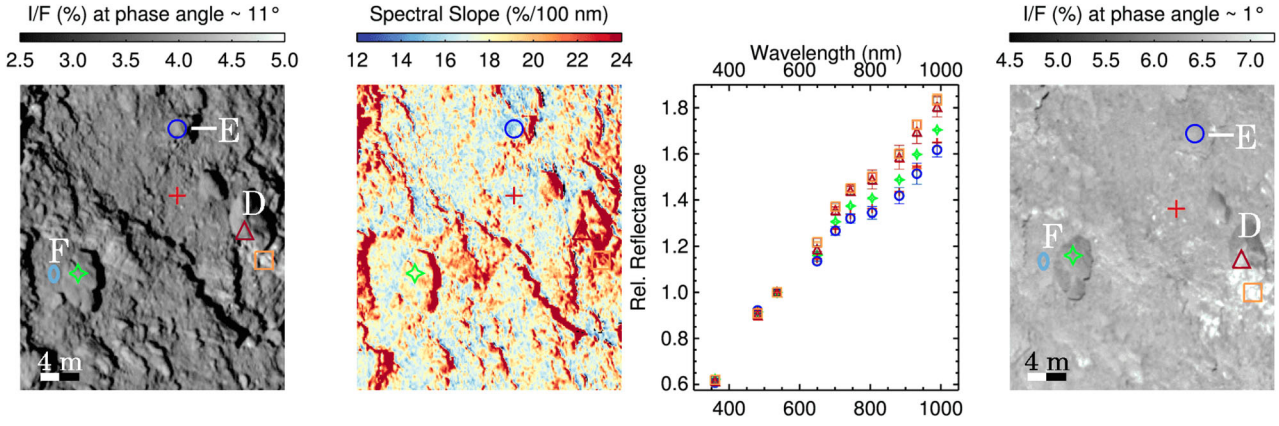

Figure 9. From left to right: radiance factor of ROI 3, associated spectral slope map (evaluated in the 743–535 nm range) and spectrophotometry for five selected features at phase angle 11° (NAC orange filter UTC – 12:20:54). Radiance factor at phase ∼1° (NAC orange filter UTC – 12:39:54). The phase curves of the blue ellipse and green star measurements of the 'F' boulder are presented in Fig. 13.

In those ROIs, the spectrophotometric properties of different features were investigated by integrating the radiance factor, on Lommel–Seelinger disc-corrected images, inside squared boxes of 3×3 pixels (i.e. about 0.33×0.33 m^2).

The spectrophotometric measurements in ROI 1 (cf. Fig. 7) indicate that boulder named A is very red in term of spectral slope [$S = 22.5$ per cent/(100 nm)]. Its brighter side, indicated by the brown triangle, is spectrally redder than the darker regions of the same boulder, indicated by the blue circle, and as red as the nearby boulder on its left (green star). The bright spot marked by the violet triangle has a spectral slope less steep than that of boulder A [$S =$ 20 per cent/(100 nm)], but it is still redder compared to the relatively smooth regions indicated by the red cross and orange square, whose spectral slope value is around 19 per cent/(100 nm). The

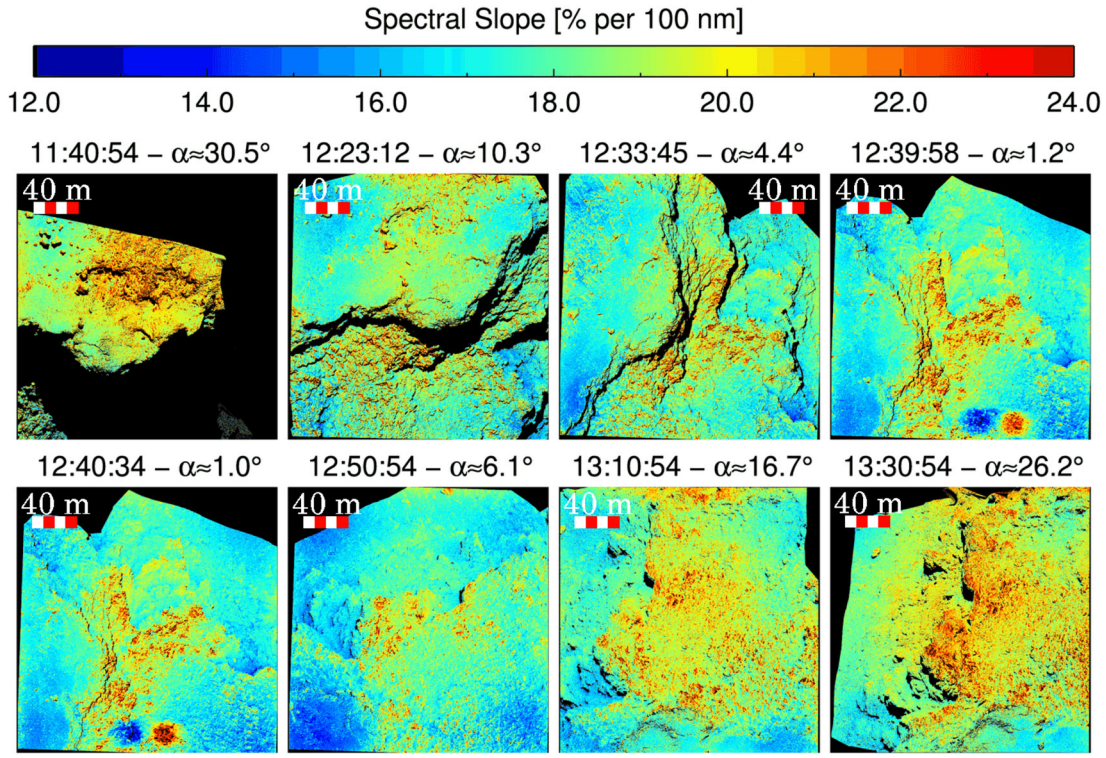

Figure 10. Panel of spectral slope mappings in the 743–535 nm range at selected times of the fly-by. The epochs indicated are in UTC. As in Fig. 3, the areas in black correspond either to shadows or to areas not defined in the employed 3D model of the region.

behaviour of this surface element, i.e. high reflectance and also steep spectral slope, is completely different compared to what previously observed by Fornasier et al. (2015), Pommerol et al. (2015b), Fornasier et al. (2016), Barucci et al. (2016) and Oklay et al. (2016). In those papers, the authors observed bright features on Hapi and in other locations over the nucleus, which were associated with a small spectral slope value [$S < 10$ per cent/(100 nm)]. This behaviour, i.e. high reflectance and moderate spectral slope value, was linked to the presence of water-ice mixed to refractory material. We surmise that the red spectral slope of the bright feature in ROI 1 could be explained through a difference in terms of composition: this feature would not be enriched in water-ice but probably rather in minerals brighter than the surroundings dark agglomerate. But it could also point out to a difference of texture: this feature might be smoother or have a lower porosity than its surroundings.

Additionally in this ROI, we observe that the top of A boulder (blue circle) has a spectral behaviour similar to that of the surface layer at its feet (red cross) indicating that both are covered by similar dark and red dust material.

The area contained in ROI 2 (cf. Fig. 8) displays higher variations in the spectral behaviour compared to ROI 1, including both red features such as the one named B [$S = 21.7$ per cent/(100mn)], and bluer regions such as the one named C [$S = 15$ per cent/(100mn)]. Strata-head B is characterized by a steep spectral slope in the 650–1000 nm range (see the red cross symbol on Fig. 8) among the investigated areas. The measurement on the outcrop named C (where the orange square is placed) has a slightly higher radiance factor than the average in ROI 2 together with a bluer spectral behaviour than the surroundings.

The two metre-sized boulders located beneath the green cross and brown triangle have a spectral behaviour indistinguishable from the smoother region indicated by the blue circle, again pointing towards a similar composition in the uppermost dust layer.

In ROI 3, we have investigated two metre-scaled boulders which show again a lower opposition effect at small phase angles, designated D and F in Fig. 9 together with another boulder, named E, whose reflectance is indistinguishable from the surroundings at small phase angle. This region shows spectral slope variations as high as in ROI 2. Particularly interesting is feature D, which entails some bright patches at the feet of the boulder. The reflectance of those patches is up to 40 per cent higher than the boulder's. Despite the reflectance variation, both dark and bright components of boulder D show a similar very red spectral behaviour, redder than smooth surrounding regions (as the one indicated by the red cross) or of F and E boulders.

Our interpretation is that, possibly due to thermal stress, the sombre boulder has fractured and released chunks of fresh material that now constitute the bright patches. Both bright patches and boulder might have been later coated with organic-laced dust, and therefore exhibit such a red spectral slope (see Fig. 4d).

5.1 Phase reddening

We plotted the spectral slope values versus the phase angle for each pixel of the available images is represented in Fig. 11.

The phase-reddening phenomenon is evident but characterized by a lower slope compared to the previous measurements (Fornasier et al. 2015): a linear regression of this data set gave us a slope of $\beta = (0.0652 \pm 0.0001) \times 10^{-04}$ nm^{-1} deg^{-1} and the spectral slope at zero phase angle is estimated to be (17.9 ± 0.1) per cent/(100 nm) in the 743–535 nm range.

We note that Fornasier et al. (2016) also reported a strong decrease of the phase-reddening effect comparing the spectral slope values

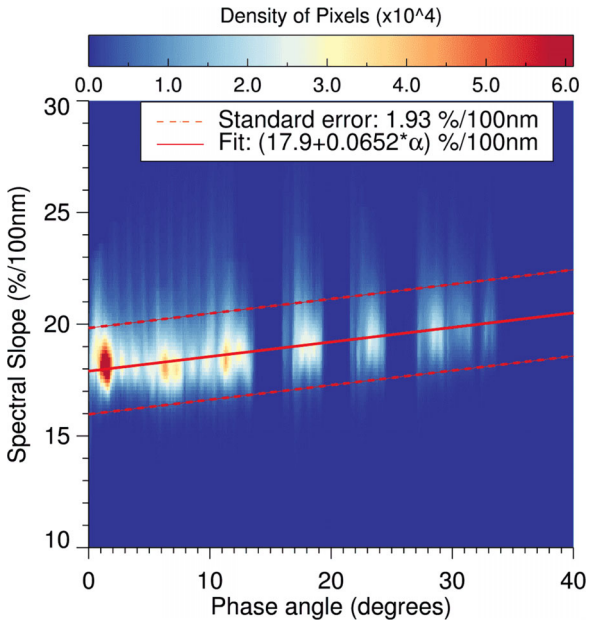

Figure 11. Spectral slope values versus phase angle. The red line corresponds to the linear regression of the spectral slope as a function of phase angle, while the dashed lines correspond to the standard deviation.

averaged over the comet rotational period from 2014 August data sets ($\beta = 0.104 \cdot 10^{-04}$ nm^{-1} deg^{-1}) and those acquired from 2015 April to August ($\beta = 0.041 \times 10^{-04}$ nm^{-1} deg^{-1}), when the comet approached and passed through its perihelion. They explain the decrease of the phase-reddening effect as a result of the increasing level of activity that progressively removed the dust mantle. The fly-by data have intermediate phase-reddening value comparable to those analysed in Fornasier et al. (2016). This can be interpreted as progressive dust mantle removal – as the activity increases at lower heliocentric distance – with changes of the surface properties, like the dust roughness or the uppermost layers composition.

6 PHOTOMETRIC ANALYSIS

In order to compare our results with the literature, we choose to apply the Hapke radiative transfer model to fit our data set for the purpose of this study.

6.1 Hapke model and inversion procedure

The latest equation of Hapke model, in radiance factor, is defined by the expression:

$$\mathrm{RADF}(\lambda, \mu_0, \mu, \alpha) = K \frac{w_\lambda}{4} \left(\frac{\mu_{0e}}{\mu_e + \mu_{0e}} \right) \times [(1 + B_{\mathrm{SH}(\alpha)}) p_{(\alpha)} + (1 + B_{\mathrm{CB}(\mu_0,\mu,\alpha)})(H_{(\mu_0/K,w_\lambda)} H_{(\mu/K,w_\lambda)} - 1)] \times S_{(\mu_0,\mu,\alpha)}, \quad (4)$$

where μ_{0e} and μ_e are the effective cosine of incidence and emergence angles, involving the topographic correction of the facet by the macro-roughness shadowing function S.

K is the porosity factor, w_λ is the single-scattering albedo (or SSA), B_{SH} is the shadow-hiding opposition effect (SHOE) term, p is the single or double lobe Heyney–Greenstein particle phase function (or SPPF), B_{CB} is the coherent-backscattering opposition effect (CBOE; Akkermans et al. 1988) term and H is the isotropic multiple scattering approximation function, analytically described by the second-order approximative Ambartsumian–Chandrasekhar function (Hapke 2002). Table 3 presents the free Hapke parameters and their respective relationship with the scattering curve morphology and properties of the surface. We name this version as Helfenstein–Hapke–Shkuratov model (hereafter noted HHS model). A further qualitative and mathematical description of the photometric model and its functions can be found in Helfenstein & Shepard (2011) or Hapke (2012).

For data inversion we proceed as follows: first, a table of facets for each image is binned into a 50 × 50 × 50 (125.000) cell grid [in steps of 1.°5 × 1.°5 × (0.°05), which translates in to shells of 0.3 m in diameter] in respect to i (incidence), e (emergence) and α (phase) angles. The RADF is averaged for each cell, mitigating any effect of variegation and poor pixels/facets. Cells with no pixels are removed from data. Then, the fitting procedure is focused on minimizing the χ^2 between the measured and modelled RADF weighted by the number of facets on each active cell. 30 initial conditions of lowest χ^2 are selected from 1000 random initial conditions (search grid of 0.01 interval) to undertake thorough minimization by the Broyden–Fletcher–Goldfarb–Shanno (L-BFGS-B) algorithm (Broyden 1970; Zhu et al. 1997), available by SCIPY PYTHON package (Van Der Walt, Colbert & Varoquaux 2011). L-BFGS-B solves non-linear problems by approximating the first and second derivatives in an iterative procedure to search for local solution. Finally, the 30 Hapke solu-

Table 3. Description of the Hapke parameters.

Parameter	Description	Bounds
w_λ	Particle single-scattering albedo (SSA).	{0.01, 0.5}
$g_{\mathrm{sca},\lambda}$	Asymmetric factor. Coefficient of the mono-lobe Heyney-Greenstein function. The average cosine of emergence angle of the single particle phase function (SPPF).	{−1.0, 1.0}
K	Porosity factor $K = \ln(1 - 1.209\phi^{2/3})/1.209\phi^{2/3}$, ϕ is the filling factor. It is an addition introduced by Hapke (2008) corresponding to the role of superficial porosity in the scattering. The porosity factor and h_s are constrained through the approximative formula $K = 1.069 + 2.109h_s + 0.577h_s^2 - 0.062h_s^2$	{1.0, 1.7}
Bs_0, h_s	Amplitude and angular width of the SHOE. h_s relates with micro-roughness and porosity. Bs_0 is a function of the specular component of the Fresnel reflectance $S(0)$.	{0.0, 3.0}, {0.0, 0.15}
Bc_0, h_c	Amplitude and angular width of the CBOE. $h_c = \frac{\lambda}{2\pi l}$, thus h_c is inversely proportional to the mean photon path l. Bc_0 is somehow connect to the particle scattering matrix.	{0.0, 1.0}, {0.0, 0.15}
$\bar{\theta}$	Average macroscopic roughness slope of sub-pixel/sub-facet scale.	{1°, 90°}

Table 4. Hapke parameters for the 2015 February fly-by area.

Model	Filter	w_λ (±0.001)	g_{sca_λ} (±0.02)	$B_{\mathrm{SH},0}$ (±0.3)	h_{SH} (±0.005)	$\overline{\theta}$ (deg) (±0.2)	K (±0.005)	Porosity	p_v
H2002[a]	*F*82	0.042	−0.37	2.5	0.079	15	–	–	0.064
H2002[b]	*F*84	0.032	−0.39	2.57	0.067	16.5	–	–	0.052
H2002	*F*82	0.046	−0.37	2.56	0.064	15.6	–	–	0.068
H2002	*F*88	0.053	−0.36	2.52	0.064	15.1	–	–	0.079
HHS[a]	*F*82	0.034	−0.42	2.25	0.061	28	1.20	0.87	0.067
HHS[c]	*F*84	0.026	−0.39	2.56	0.067	16.3	1.226	0.85	0.052
HHS	*F*82	0.038	−0.37	2.57	0.064	15.6	1.219	0.86	0.068
HHS	*F*88	0.044	−0.36	2.64	0.066	15.2	1.212	0.85	0.079

[a]Obtained by (Fornasier et al. 2015), from OSIRIS data.
[b]Hapke (2002) model.
[c]HHS model (see Section 6.1).

tions are averaged to obtain the final solution and the uncertainties tied to each Hapke parameter.

The photometric phase curve of the area, sampled between 0.°2 and 33°, shows a similar behaviour in the three filters investigated (NAC *F*82, NAC *F*84 and NAC *F*88): linear up to $\alpha \approx 5°$, slightly non-linear up to $\alpha = 0.°2$ and without any obvious sign of sharp spike at close opposition. We considered all the pixels covered by the shape model at *i* and *e* smaller than 80°. We also further excluded those affected by the spacecraft shadow, i.e. $\alpha \leq 0.2$. Thus, we used a total of 25 NAC *F*82, 24 NAC *F*84 and 23 NAC *F*88 images, which amounts to respectively, a total of 650 810, 633 674 and 647 776 active cells, reaching phase angles low enough to constrain the CBOE parameters. Most of the RADF spread is accounted by the assorted illumination conditions, while some few scattered cells are due to the poor description of the shape model for certain terrain slopes or overshadowed facets.

The HHS model has a maximum of 10 free parameters to be adjusted when the photometric sampling has a large enough coverage, i.e. from 0° to ∼90° for the *i* and *e* angles, and α from 0° to ∼180°. However, the fly-by data are limited to $\alpha \leq 33°$, leading us to apply only the single-term Heyney–Greenstein function to describe the backscattering lobe of the particle phase function. By also taking into account the approximative expression between h_s and K parameters (Table 4, Helfenstein & Shepard 2011), we end up with seven free parameters.

Role of the CBOE term

The coherent-backscattering mechanism rises from intergrain–intragrain multiple scattering of secondary and higher orders. During our modelling, the first iteration of the inversion procedure revealed that CBOE parameters do not gradually converge on Hapke (2002) or HHS models to a single solution, which points out to redundancy of this mathematical addendum when a second opposition spike is not verified. This has also been emphasized in our analysis of the first approaching images of the whole Northern hemisphere (Fornasier et al. 2015). Thus, visual inspection of phase curve have shown no presence of any sharp opposition spike to $\alpha \leq 0.2$. Shepard & Helfenstein (2007) have also found out CBOE is negligible when analysing samples with Hapke (2002) model. Therefore, considering that coherent-backscattering is not expected to play a major role in the opposition effect of high absorbance surfaces (Shevchenko & Belskaya 2010; Shevchenko et al. 2012), such as the cometary carbon-rich mantles, we decided to remove it from our final Hapke analysis. We note that also Masoumzadeh et al. (2016) found the coherent back-scattering mechanism negligible in their analysis of the 2015 February 14 data of the 67P/CG comet.

6.2 Results

We fit to the three filters the five-parametric Hapke (2002) model and HHS model. For all of them, the models have successfully converged to a single solution. Fig. 12 shows the observations together with the Hapke modelling for the three filters and the associated rms. The total deviation of the modelled RADF compared to measured quantities (red line, Fig. 12a–c) is no higher than 4.8 per cent, reaching almost 1:1 ratio in respect to the small phase angles images (black line). The best Hapke parameters found for the different filters reproduce correctly variations due to illumination conditions.

The final Hapke solutions are shown in Table 4, together with pre-perihelion solutions obtained from the OSIRIS images from 2014 July 21 to August 6 ($1.°3 < \alpha < 54°$, Fornasier et al. 2015). The parameters solution derived for the Ash–Imhotep area are very similar to those retrieved for the whole Northern hemisphere. The area has a very small SSA, medium backscattering particle phase function, strong shadow-hiding mechanism, high top-layer porosity and smooth macroscopic roughness. Ciarniello et al. (2015), modelling the VIRTIS-M data of the 67P/CG comet for $27.°2 < \alpha < 111.°5$ from 2014 July to 2015 February, obtained higher w (0.06 ± 0.01) and g_{sca} (-0.42) values, but a $\overline{\theta}$ value consistent with our work. The discrepancies in the results between OSIRIS and VIRTIS data are related to the different phase angle range used to compute the phase curve slope, and to the different forms of Hapke modelling adopted. Indeed, Ciarniello et al. (2015) neglected the opposition effect in their modelling. This results in a steeper (more negative) g_{sca} value to account for the slope caused by opposition effect, and a steeper phase function that requires a higher SSA value to compensate for the overall measured I/F scale.

Rosetta provides for the first time the opportunity to derive the full set of parameters for a comet nucleus, particularly for the opposition effect regime (hereafter OE), as all the other cometary nuclei visited by spacecraft have been observed at $\alpha > 11°$. The surface analysed here and in Fornasier et al. (2015) is characterized by a large B_{s0} parameter, where according to Hapke (2012), SHOE amplitudes higher than the nominal limit of 1.0 might indicate the presence of sub-particle structures, casting shadows on to one another, which would cause SHOE mechanism to be further enhanced. As most part of the top surface of 67P/CG is possibly covered by resettled fluffy dust layer in the low-gravity environment, it is not unpredictable that mutual shadow hiding among particles should not be an enhanced mechanism. Furthermore, the superficial

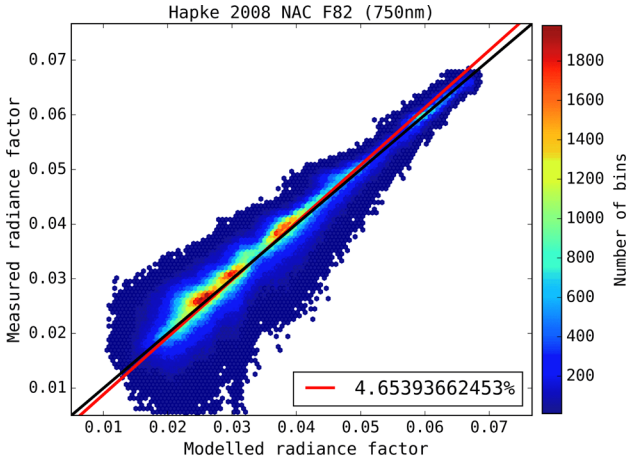

(a) Goodness fit of the NAC F82 data

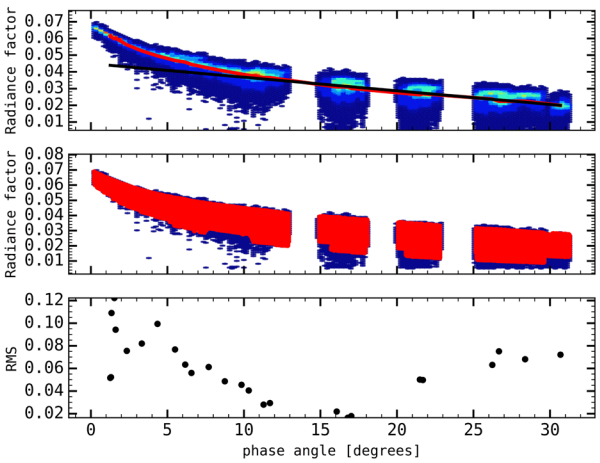

(d) Fitting, simulation and corresponding RMS for the NAC F82 data

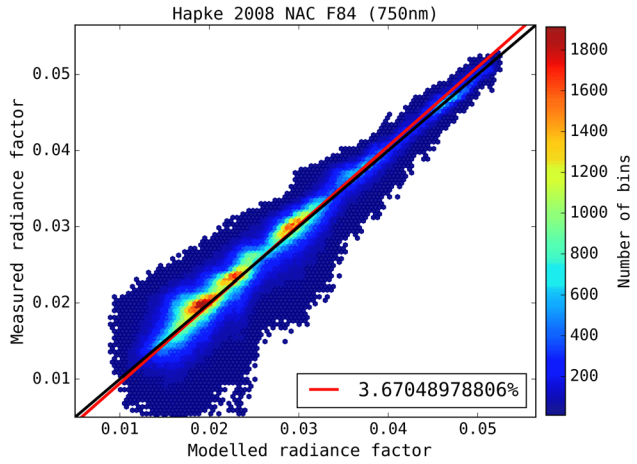

(b) Goodness fit of the NAC F84 data

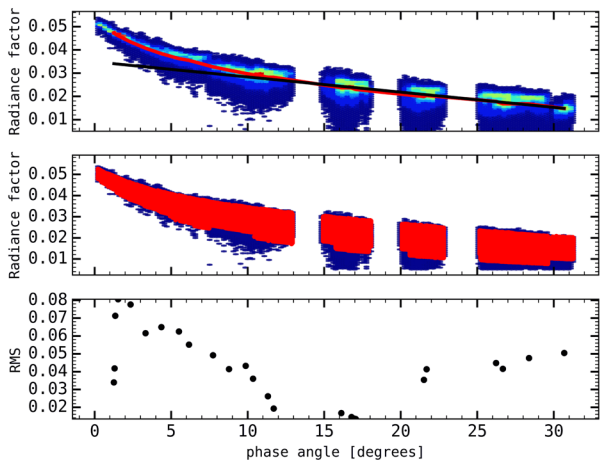

(e) Fitting, simulation and corresponding RMS for the NAC F84 data

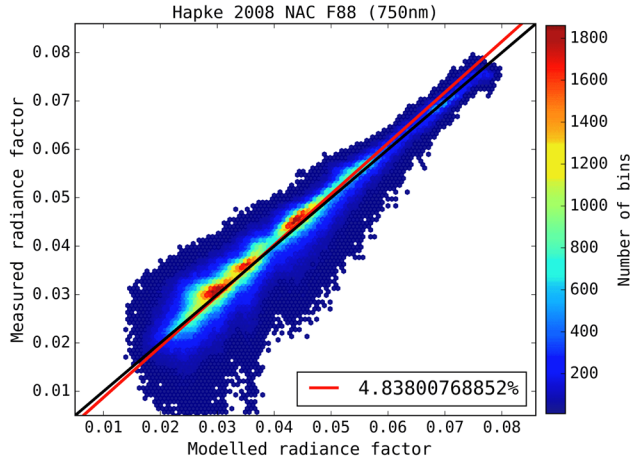

(c) Goodness fit of the NAC F88 data

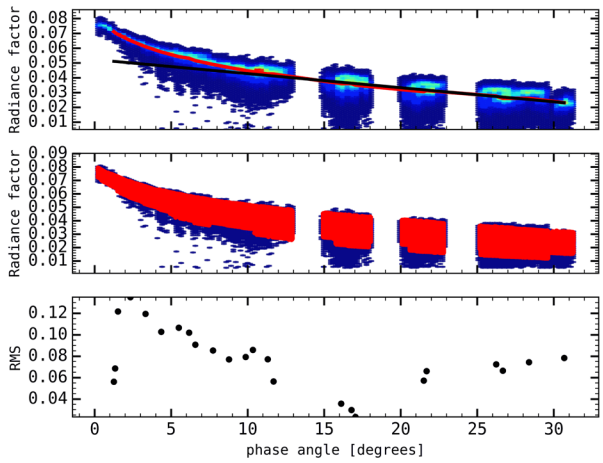

(f) Fitting, simulation and corresponding RMS for the NAC F88 data

Figure 12. Figures from the Hapke modelling. On the left-hand side, the three figures depicts for all three filters the measured RADF versus the modelled RADF. The black line represent a slope of 1 (i.e. a perfect match). The red line is our best linear fit by taking into account all active cells. On the right-hand side, the three panels of figures present the results of the photometric modelling for each NAC filter. In each figure, the diagram at the top corresponds to the phase function in the corresponding filter with the curve being the best-fitting solution of the photometric modelling. The diagram in the middle presents an overplot of the same phase function with the simulation of the data set using the 3D model and the best-fitting solution. Finally, the diagram at the bottom displays the mean of the rms for each image. In all of these figures, as the measured radiance factor values have been binned, the first and second diagrams show a underplotted density distribution of the active cells.

porosity of the Ash–Imhotep region (86 per cent) is indistinguishable compared to that derived for the Northern hemisphere. This high value is similar to the one determined by the Philae measurements for the first tens of metres during the first rebound on the comet (75–85 per cent, Kofman et al. 2015), and in agreement with the porosity value of fractal aggregates (Bertini, Thomas & Barbieri 2007; Levasseur-Regourd et al. 2007; Lasue et al. 2011) that are believed to be the best analogues of cometary dust. Low thermal inertia and high micro-roughness are proxy physical quantities to a high superficial porosity and a sharper SHOE. Laboratory experiments predict such correlation (Zimbelman 1986; Piqueux & Christensen 2009). Therefore, as expected, our results are in agreement with high micro-roughness ($\overline{\theta_r} \approx 55^\circ$, Kamoun et al. 2014) obtained through re-analysis of radar echo from Arecibo observatory and the low thermal inertia of $\sim 85\,\mathrm{J\,m^{-2}\,K^{-1}\,s^{-1/2}}$ provided by MUPUS instrument on-board Philae (Spohn et al. 2015).

Briefly, w, g_{sca}, $\overline{\theta}$ and ρ_v are the only Hapke (2002) parameters that can be compared to the literature. The Ash–Imhotep area along with all the Northern hemisphere (Ciarniello et al. 2015; Fornasier et al. 2015) shows similar photometric behaviour to other nuclei in the visible spectral range, specially 9P/Tempel 1 ($w_{650\,\mathrm{nm}} = 0.039$, $g_{\mathrm{sca}} = -0.49$, $\overline{\theta} = 16^\circ \pm 8^\circ$ and $\rho_v = 0.059$, Li et al. 2007a) and 103P/Hartley 2 ($w_{750\,\mathrm{nm}} = 0.036$, $g_{\mathrm{sca}} = -0.46$, $\overline{\theta} = 15^\circ \pm 10^\circ$ and $\rho_v = 0.045$, Li et al. 2013). The geometric albedo ρ_v of the 67P/CG nucleus has an intermediate value compared to that found for 81P/Wild 2 ($\rho_v = 0.059$, Li et al. 2009) and 19P/Borrelly ($\rho_v = 0.072 \pm 0.002$, Li et al. 2007b). Moreover, 67P/CG shows g_{sca} lower than all other nuclei. None of previous spacecraft comets attained the same spatial resolution than *Rosetta* in their cometary images. However, both objects that present similar Hapke parameters, Tempel 1 and Hartley 2, are those that also demonstrate overflow of extremely smooth and fine material in their surface, in a comparable manner to the Hapi region on 67P/CG.

6.3 Investigation of bright patches and dark boulders

As mentioned in Section 4, the Fig. 13 shows the phase curves of four selected areas which have different morphology, including a sombre boulder and a bright spot. The bright spot investigated here corresponds to the violet triangle in Fig. 7, while the sombre boulder corresponds to the feature F in Fig. 9. As expected, we observe that the reflectance of this feature, which appears bright under every illumination conditions in every image, is larger than that of the dark boulder. We also note, for the bright spot, that the OE surge at small phase angle is not pronounced as what could be expected in the case of water-ice rich material. We also report that the dimensions of the dark boulder are only merely above the vertical and horizontal accuracy of the 3D model of the region: hence though this feature is visible in the 3D model, its reconstitution lead to a disparity in the generated phase angles.

The Hapke parameters for the bright spot and the dark boulder present a clear dichotomy between the two objects (see Table 5). The bright spot is characterized by a high normal and SSA and a flatter phase curve slope (g_{sca}). The reverse is measured for the dark boulder. As the phase curve slope is inversely proportional to the

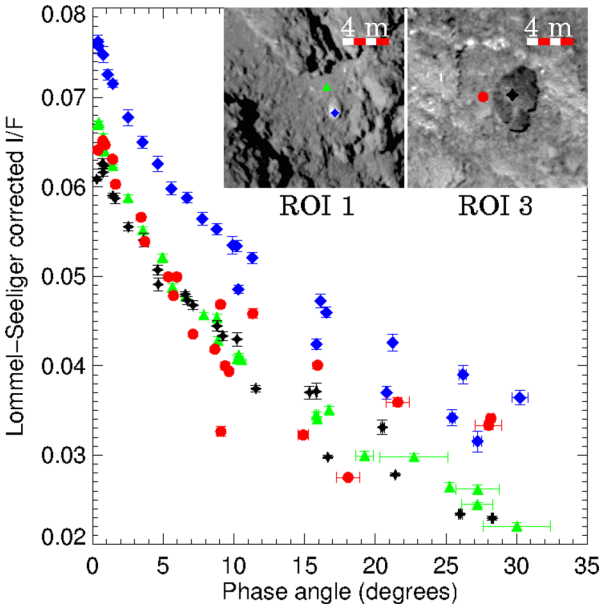

Figure 13. Phase curves at 649 nm of a bright spot (the violet triangle in Fig. 7), of a dark boulder (the green star in Fig. 9) and their respective contiguous terrains (orange square in Fig. 7) and the base of feature F in ROI3 (its position is indicated with the blue ellipse in Fig. 9).

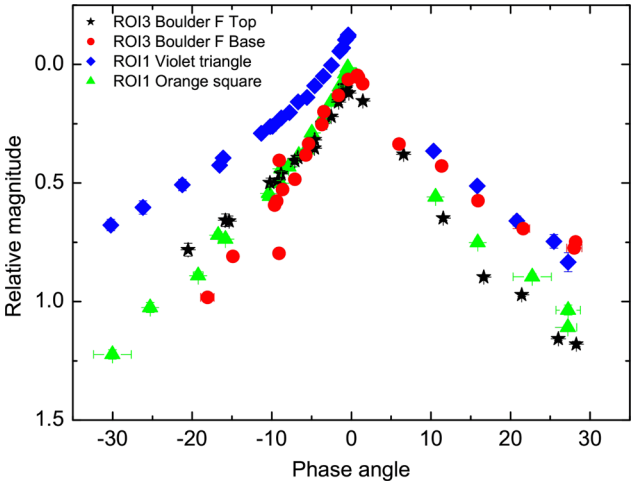

Figure 14. Diagram of the difference in magnitude for the phase curves at 649 nm of the four selected areas (cf. Fig. 13), when normalized to the averaged comet albedo (6.8 per cent).

geometric albedo (Déau et al. 2013), the same SHOE width and amplitude might indicate that the micro-roughness structure in the top layers is preserved.

The radiance factor values normalized to the averaged comet albedo (0.068) and converted to magnitudes, are presented in Fig. 14. One of the considered areas (violet triangle in Fig. 7) is noticeably brighter while other three areas have similar albedos. An asymmetry of phase curves measured before and after opposition is

Table 5. Results of HHS modelling for the two outstanding surface elements investigated.

Feature	$w_{649\,\mathrm{nm}}$	g_{SCA}	$B_{\mathrm{SH},0}$	h_{SH}	Porosity	p_v
Bright spot (ROI 1)	0.067 ± 0.004	-0.26 ± 0.07	2.07 ± 0.61	0.103 ± 0.025	0.81 ± 0.02	0.077
Sombre boulder F (ROI 3)	0.029 ± 0.004	-0.41 ± 0.06	2.27 ± 0.75	0.108 ± 0.034	0.82 ± 0.02	0.064

well seen. It becomes evident at a phase angle larger than 10°–15° and can be most probably explained by variations of local elevation. The surface at the base of the ROI1's bright spot, which appears as a more regular surface, shows the smallest difference between phase curves before and after opposition.

To compare phase behaviours of selected areas, we considered only phase angles up to 10° where an influence of the relief is less significant. The brighter region exhibits a distinct OE as contrary to darker regions, for which the magnitude-phase dependences are linear at small phase angles. The linear phase slopes are 0.045 ± 0.002 mag deg^{-1} (green star at the top of boulder F in Fig. 9), 0.062 ± 0.005 mag deg^{-1} (blue ellipse at the feet of boulder F) and 0.051 ± 0.002 mag deg^{-1} (orange square at the base of the bright spot in Fig. 7). The differences in phase slopes are most probably related to the variation of surface roughness. The boulder which looks darker than its surroundings should have considerably smoother surface compared to the surface at its base.

The values of phase slopes found for selected areas of the comet are within typical values observed for comets (e.g. Li et al. 2007b), and in particular similar to what has been found for the global 67P/CG (0.047 ± 0.002 mag deg^{-1} for $\alpha > 7°$) from early resolved images of the nucleus (Fornasier et al. 2015), and in particular for the sombre boulder and the smooth Ash terrain.

6.4 Comparison to radio-goniometric measurements

The 2015 February fly-by provides the first-time opportunity to retrieve and analyse photometric parameters at spatial resolution comparable to those obtained through laboratory experiments. Recently, in the framework of *Rosetta* mission, new spectro-photometric measurements on cometary analogues were performed at the University of Bern using the PHIRE-2 radio-goniometer and the SCITEAS simulation chamber (Pommerol et al. 2011, 2015a,b; Jost et al. 2016). The PHIRE-2 radio-goniometer measured the scattering curve before and after sublimation of intermixture/intramixture samples of 67 ± 31 μm ice particles, 0.2 wt per cent carbon black and 0.1 wt per cent tholins at 750 nm. The intermixtures and intramixtures are produced using different sample preparation protocols and differ by the structure of the sample at the scale of the individual grains. The dust and water-ice grains are individually separated in the intermixture, whereas minerals grains are contained inside the water-ice grains for intramixture preparations. Each experiment was set up into a 2 × 4 × 2 cm^3 sample holder, providing four combinations of cometary analogue surfaces plus an ice-less combination of tholins (33 per cent) and carbon black (66 per cent), we refer the reader to Poch et al. (2016a) for more details on the preparation methods. The resolution of comet data from the 2015 February fly-by is of 11cm pixel^{-1}, whereas the analogue surfaces are about only 10 times smaller, placing them as an equivalent to the highest resolved surface unit of 67P/CG up to now.

As the cometary surfaces investigated here are essentially ice-free, we compare the photometric properties derived from NAC *F*88 fly-by data to laboratory data obtained for the fully sublimated state of three different types of cometary surfaces analogues (Jost et al., in preparation). The laboratory reflectance data were measured with the PHIRE-2 radio-goniometer at a central wavelength of 750 nm. The comparison, as presented in Fig. 15(a) for incidence angle equal to zero, clearly indicates that the sublimated 'intramixture' sample (see Fig. 15b) displays a similar scattering curve in the phase angle range of the fly-by. The three samples show quite similar phase curve slope, whereas intermixture is slightly flatter than intramixture for $\alpha > 15°$. None the less, the intramixture is the only sample to fit the 67P/CG phase curve in absolute radiance factor and also in slope.

At larger phase angles ($\alpha \gtrsim 40°$), the intramixture scattering curve becomes wider and strongly forward scattering, which is very different from what is observed by Ciarniello et al. (2015) for $\alpha > 80°$, where the overall reflectance goes fainter. This is essentially due to the effect of large-scale topography and roughness that are absent from the laboratory samples but dominate the photometry of the nucleus at these large phase angle. Moreover, radiometric measurements were not obtained to $\alpha < 5°$, which does not allow us to infer the shape and magnitude of the opposition surge.

According to Poch et al. (2016b), an intramixed surface has as characteristic the formation of mantles of high internal cohesiveness and with episodic and bigger release of fragments during sublimation than intermixed counterpart. Under the optical coherence tomographic scan (Jost et al., in preparation), intramixtures also present a higher superficial roughness than intermixtures, which would also indicate an higher superficial porosity, as found by the photometric

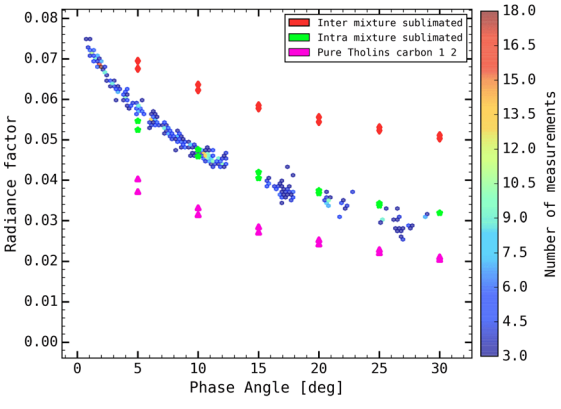

(a) laboratory experiments comparison

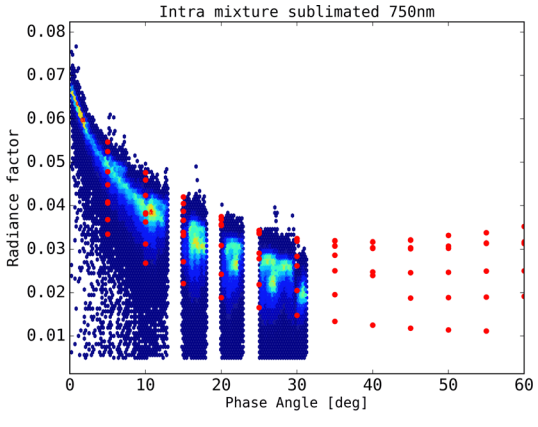

(b) laboratory experiments comparison

Figure 15. (a) Comparison phase curves of dry laboratory samples and NAC *F*88 fly-by area for phase angle smaller than 35° at 750 nm. For both data, it was selected measurements at incidence angle equal to zero. The dry samples are the sublimated intramixtures and intermixtures, and an assemblage of tholins (33 per cent)+carbon black(66 per cent). (b) Best match: sublimated intramixture. The scatter of measurements well represent the disc behaviour observed in the fly-by phase curve. The lack points at $\alpha < 5°$do not allow us to infer any information about the opposition surge.

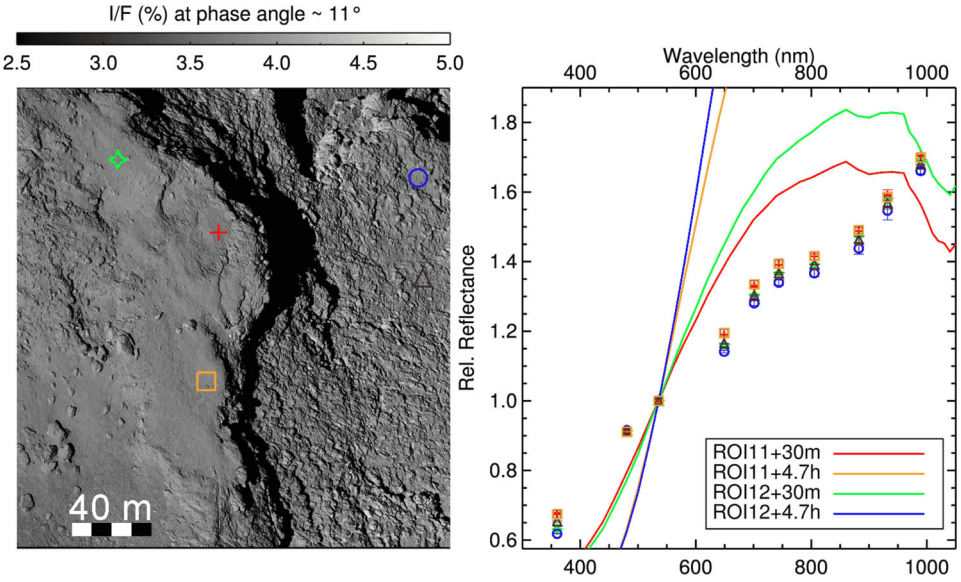

Figure 16. Comparison with laboratory measurements: the ROIs of the legend refer to those defined in Poch et al. (2016b), while the time indicated refers to the lapse of time the samples were left to sublimate.

modelling of the comet.[2] However, none of these surface properties have been quantitatively characterized yet.

7 DISCUSSIONS AND OUTLOOK

The analysis of the decimetre-scaled observations of the comet 67P/CG with the OSIRIS instrument reveals that the photometric parameters of the flown-by region are similar to those of the whole nucleus. The comet surface is noticeably dark, its uppermost layer is very porous, and it preferentially backscatters the reflected light (see Table 4). The spectrophotometric analysis of smooth and dusty area on both Ash and Imhotep regions indicates similar properties in terms of texture and composition. These terrains are found to be among the reddest in term of spectral slope on the comet surface. We note here that the texture of the material covering the Ash part of the flown-by region appears similar to the observations of the ROLIS instrument on-board the Philae lander, as presented in Mottola et al. (2015). We also observe similar textures in parts of the flown-by region: a smooth regolith with the presence of decimetre and metre-sized boulders, alone or as part of clusters, and alcoves.

However, the spectrophotometric analysis also points out to local variations in terms of reflectance and colours (respectively, up to 40 per cent and 50 per cent) pointing to local heterogeneities at the metre and decimetre scale associated with peculiar morphological features such as boulders. Heterogeneities were confirmed at larger scales by OSIRIS and at smaller scales by the CIVA instrument onboard Philae (Bibring et al. 2015), both in terms of texture and composition.

In their study of the Agilkia region (where the Philae lander made its first touchdown), La Forgia et al. (2015) found that the area closest to outcrops and cliffs were those exhibiting the reddest spectral behaviour, which is in agreement with our observations of Fig. 10. Furthermore, they also investigated the spectrophotometric difference between fine deposits and outcrops area, and they found that fine deposits have a relatively bluer spectrum than outcrops, a result which is in agreement with our observations in the different ROIs.

The presence and origin of fine deposits in the Agilkia and Ash regions have already been investigated and discussed in Thomas et al. (2015a); La Forgia et al. (2015): the authors speculate that those fine deposits might be the results of airfall of material originating from other active regions, such as Hapi.

The investigation of the origin of fine deposits in the fly-by region is beyond the scope of this paper, yet we can retain that an airfall hypothesis could explain why the top of outcrops and boulders have a spectral behaviour similar to pebble-less neighbouring surfaces.

When investigating the median spectral slope of the area flown-by, and the spectra of large boulder-less surfaces (1.5×1.5 m^2), as in La Forgia et al. (2015), we found likewise that the surface was revealing a global red spectral behaviour ($S_{\rm med} = 17.7$ per cent/100 nm at 1° of phase angle) without any evidence of absorption features (with the exception of the cometary emission overflux) in the near-UV to near-IR domain. According to VIRTIS results, the red spectral behaviour is compatible with an organic-rich composition (Capaccioni et al. 2015; Filacchione et al. 2016).

When comparing our data set to Jost et al. (2016), we found that a intramixture composed of tholins and of carbon black was a best match in terms of photometric properties. However, when comparing spectra of fresh and sublimated samples of intramixture and intermixture of water-ice, tholins and minerals (olivine and smectite), we found that no sample would match well the spectrophotometric properties of the surface layer of the flown-by region, as depicted in Fig. 16.

Reflecting that such samples are not a proxy for the comet's composition, we can nevertheless remark that the after-sublimation intramixture sample was a better match than the intermixture sample in terms of photometric properties.

As we have previously mentioned, in this region, the bright spots display a steep spectral slope value, which is not normally associated

[2] Optical coherence tomographic scans of the residues obtained after sublimation of intramixture and intermixture ice/dust samples are published in Poch et al. (2016b).

with terrains enriched in water-ice on the comet 67P/CG. Moreover, the reflectances of the bright spot are not as high (three to eight times the reflectance of the surroundings) as normally observed in exposed water-ice spots on the comet (Pommerol et al. 2015b; Barucci et al. 2016; Fornasier et al. 2016).

All of the observed boulders of the flown-by region showing a lower reflectance at small phase angle, relative to their surroundings, also exhibit a red spectral behaviour, often much redder than the surroundings. However, also brighter regions in or close to the dark boulders, like the one observed on boulders A or F often show a red spectral behaviour very close to that of the darker boulders. This indicates that the uppermost composition must be similar in the aforementioned structures, and that the different reflectance may be related to grain size properties, with brightest features having probably smaller grain size.

Yet, those measurements give an extraordinary insight at the decimetre-scaled structure of the nucleus and surely a preview of the upcoming OSIRIS observations as the *Rosetta* spacecraft will orbit, in the coming months, closer and closer to the nucleus of comet 67P/CG.

ACKNOWLEDGEMENTS

OSIRIS was built by a consortium of the Max-Planck-Institut für Sonnensystemforschung, Göttingen, Germany, CISAS–University of Padova, Italy, the Laboratoire d'Astrophysique de Marseille, France, the Instituto de Astrofísica de Andalucia, CSIC, Granada, Spain, the Research and Scientific Support Department of the European Space Agency, Noordwijk, the Netherlands, the Instituto Nacional de Técnica Aeroespacial, Madrid, Spain, the Universidad Politéchnica de Madrid, Spain, the Department of Physics and Astronomy of Uppsala University, Sweden, and the Institut für Datentechnik und Kommunikationsnetze der Technischen Universität Braunschweig, Germany. The support of the national funding agencies of Germany (DLR), France (CNES), Italy (ASI), Spain (MEC), Sweden (SNSB) and the ESA Technical Directorate is gratefully acknowledged.

Rosetta is an ESA mission with contributions from its member states and NASA. Rosetta's Philae lander is provided by a consortium led by DLR, MPS, CNES and ASI.

The SPICE, SPICE/DSK libraries and PDS resources are developed and maintained by NASA. The authors wish to thank Nathan Bachmann and his colleagues for their guidance.

REFERENCES

A'Hearn M. F. et al., 2005, Science, 310, 258
A'Hearn M. F. et al., 2011, Science, 332, 1396
Acton C. H., 1996, Planet. Space Sci., 44, 65
Akkermans E., Wolf P., Maynard R., Maret G., 1988, J. Phys., 49, 77
Barucci M. A. et al., 2016, A&A, 595, A102
Barucci M. A., Dotto E., Levasseur-Regourd A. C., 2011, A&AR, 19, 48
Bertin E., 2011, Astrophysics Source Code Library, record ascl:1110.006
Bertini I., Thomas N., Barbieri C., 2007, A&A, 461, 351
Bibring J.-P. et al., 2015, Science, 349, aab0671
Broyden C. G., 1970, IMA J. Appl. Math., 6, 76
Capaccioni F. et al., 2015, Science, 347, aaa0628
Ciarniello M. et al., 2015, A&A, 583, A31
De Sanctis M. C. et al., 2015, Nature, 525, 500
Déau E., Flandes A., Spilker L. J., Petazzoni J., 2013, Icarus, 226, 1465
El-Maarry M. R. et al., 2015, A&A, 583, A26
Filacchione G. et al., 2016, Icarus, 274, 334
Fornasier S., Dotto E., Marzari F., Barucci M. A., Boehnhardt H., Hainaut O., de Bergh C., 2004, Icarus, 172, 221
Fornasier S., Dotto E., Hainaut O., Marzari F., Boehnhardt H., De Luise F., Barucci M. A., 2007, Icarus, 190, 622
Fornasier S. et al., 2009, A&A, 508, 457
Fornasier S. et al., 2015, A&A, 583, A30
Fornasier S. et al., 2016, Science, 10.1126/science.aag2671
Giacomini L. et al., 2016, Mem. Soc. Astron. Italiana, 87, 159
Hapke B., 1993, Theory of Reflectance and Emittance Spectroscopy
Hapke B., 2002, Icarus, 157, 523
Hapke B., 2012, Theory of Reflectance and Emittance Spectroscopy, 2nd edn. Cambridge Univ. Press, Cambridge
Hasselmann P. H., Barucci M. A., Fornasier S., Leyrat C., Carvano J. M., Lazzaro D., Sierks H., 2016, Icarus, 267, 135
Helfenstein P., Shepard M. K., 2011, Icarus, 215, 83
Jorda L., Spjuth S., Keller H. U., Lamy P., Llebaria A., 2010, in Computational Imaging VIII. p. 753311
Jost B., Pommerol A., Poch O., Gundlach B., Leboeuf M., Dadras M., Blum J., Thomas N., 2016, Icarus, 264, 109
Kamoun P., Lamy P. L., Toth I., Herique A., 2014, A&A, 568, A21
Keller H. U. et al., 2007, Space Sci. Rev., 128, 433
Kofman W. et al., 2015, Science, 349, aab0639
Küppers M. et al., 2007, A&A, 462, L13
La Forgia F. et al., 2015, A&A, 583, A41
Lasue J., Botet R., Levasseur-Regourd A. C., Hadamcik E., Kofman W., 2011, Icarus, 213, 369
Levasseur-Regourd A. C., Mukai T., Lasue J., Okada Y., 2007, Planet. Space Sci., 55, 1010
Li J.-Y. et al., 2007a, Icarus, 187, 41
Li J.-Y., A'Hearn M. F., McFadden L. A., Belton M. J. S., 2007b, Icarus, 188, 195
Li J.-Y., A'Hearn M. F., Farnham T. L., McFadden L. A., 2009, Icarus, 204, 209
Li J.-Y. et al., 2013, Icarus, 222, 559
Lucchetti A. et al., 2016, A&A, 585, L1
Masoumzadeh N. et al., 2016, A&A in press
Massironi M. et al., 2015, Nature, 526, 402
Mottola S. et al., 2015, Science, 349
Oklay N. et al., 2016, A&A, 586, A80
Pajola M. et al., 2015, A&A, 583, A37
Pajola M. et al., 2016, A&A, 592, A69
Piqueux S., Christensen P. R., 2009, J. Geophys. Res., 114, E09005
Poch O., Pommerol A., Jost B., Carrasco N., Szopa C., Thomas N., 2016a, Icarus, 266, 288
Poch O., Pommerol A., Jost B., Carrasco N., Szopa C., Thomas N., 2016b, Icarus, 267, 154
Pommerol A., Thomas N., Affolter M., Portyankina G., Jost B., Seiferlin K., Aye K.-M., 2011, Planet. Space Sci., 59, 1601
Pommerol A., Jost B., Poch O., El-Maarry M. R., Vuitel B., Thomas N., 2015a, Planet. Space Sci., 109, 106
Pommerol A. et al., 2015b, A&A, 583, A25
Preusker F. et al., 2015a, European Planetary Science Congress 2015, 10
Preusker F. et al., 2015b, A&A, 583, A33
Shepard M. K., Helfenstein P., 2007, J. Geophys. Res., 112, 3001
Shevchenko V. G., Belskaya I. N., 2010, in European Planetary Science Congress 2010. p. 738
Shevchenko V. G. et al., 2012, Icarus, 217, 202
Sierks H. et al., 2015, Science, 347, aaa1044
Spohn T. et al., 2015, Science, 349
Thomas N. et al., 2015a, Science, 347, aaa0440
Thomas N. et al., 2015b, A&A, 583, A17
Tubiana C. et al., 2015, A&A, 583, A46
Van Der Walt S., Colbert S. C., Varoquaux G., 2011, Comput. Sci. Eng., 13, 22
Van Der Walt S. et al., 2014, PeerJ
Vincent J.-B. et al., 2015, Nature, 523, 63

Zhu C., Byrd R. H., Lu P., Nocedal J., 1997, ACM Trans. Math. Softw., 23, 550
Zimbelman J. R., 1986, Icarus, 68, 366

[1]*LESIA, Observatoire de Paris, PSL Research University, CNRS, Univ. Paris Diderot, Sorbonne Paris Cité, UPMC Univ., Paris 06, Sorbonne Université, 5 Place J. Janssen, Meudon Cedex F-92195, France*
[2]*Deutsches Zentrum fuer Luft- und Raumfahrt (DLR), Institut fuer Planetenforschung, Asteroiden und Kometen, Rutherfordstrasse 2, D-12489 Berlin, Germany*
[3]*Aix-Marseille Université, CNRS, LAM (Laboratoire d'Astrophysique de Marseille), UMR 7326, 38 rue Frédéric Joliot-Curie, 13388 Marseille, France*
[4]*Physikalisches Institut der Universitaet Bern, Sidlerstr. 5, CH-3012 Bern, Switzerland*
[5]*Institute of Astronomy,V.N. Karazin National University, Sumska Str. 35, Kharkiv UA-61022, Ukraine*
[6]*NASA Ames Research Center, Moett Field, CA 94035, USA*
[7]*Center of Studies and Activities for Space (CISAS) 'G. Colombo', University of Padova, Via Venezia 15, I-35131 Padova, Italy*
[8]*Max-Planck-Institut für Sonnensystemforschung, Justus-von-Liebig-Weg, 3, D-37077 Goettingen, Germany*
[9]*Department of Physics and Astronomy 'Galileo Galilei', University of Padova, Vicolo dell'Osservatorio 3, I-35122 Padova, Italy*
[10]*Aix-Marseille Université, CNRS, LAM (Laboratoire d'Astrophysique de Marseille), UMR 7326, 38 rue Frédéric Joliot-Curie, F-13388 Marseille, France*
[11]*Research and Scientific Support Office, European Space Research and Technology Centre/ESA, Keplerlaan 1, Postbus 299, NL-2201 AZ Noordwijk ZH, the Netherlands*
[12]*PAS Space Research Center, Bartycka 18A, PL-00716 Warszawa, Poland*
[13]*Department of Physics and Astronomy, Uppsala University, P.O. Box 256, SE-751 05 Uppsala, Sweden*
[14]*Centro de Astrobiologia (INTA-CSIC), European Space Agency, European Space Astronomy Centre (ESAC), PO box 78, E-28691 Villanueva de la Canada, Madrid, Spain*
[15]*International Space Science Institute, Hallerstrasse 6, CH-3012 Bern, Switzerland*
[16]*Department of Astronomy, University of Maryland, College Park, MD 20742-2421, USA*
[17]*LATMOS, CNRS/UVSQ/IPSL, 11 boulevard d'Alembert,F-78280 Guyancourt, France*
[18]*INAF, Osservatorio Astronomico di Padova, Vicolo dell'Osservatorio 5, I-35122 Padova, Italy*
[19]*CNR-IFN UOS Padova LUXOR, Via Trasea, 7, I-35131 Padova, Italy*
[20]*Jet Propulsion Laboratory, M/S 183-301, 4800 Oak Grove Drive, Pasadena, CA 91109, USA*
[21]*Department of Industrial Engineering – University of Padova, via Venezia 1, I-35131 Padova, Italy*
[22]*University of Trento, Via Mesiano 77, I-38100 Trento, Italy*
[23]*INAF – Osservatorio Astronomico, Via Tiepolo 11, I-34014 Trieste, Italy*
[24]*Instituto de Astrofisica de Andalucia (CSIC), c/ Glorieta de la Astronomía s/n, E-18008 Granada, Spain*
[25]*Institut fuer Geophysik und extraterrestrische Physik (IGEP), Technische Universität Braunschweig, Mendelssohnstr. 3, D-38106 Braunschweig, Germany*
[26]*Graduate Institute of Astronomy, National Central University, 300 Chung-Da Rd, Chung-Li 32054 Taiwan*
[27]*ESA/ESAC, PO box 78, E-28691 Villanueva de la Canada, Madrid, Spain*
[28]*Department of Information Engineering, University of Padova, Via Gradenigo 6/B, I-35131 Padova, Italy*

This paper has been typeset from a TEX/LATEX file prepared by the author.